RSC Advances

PAPER

View Article Online
View Journal | View Issue

Cite this: *RSC Adv.*, 2024, **14**, 18716

Realization of a green-emitting pyrosilicate-structured Er^{3+}-activated $Y_2Si_2O_7$ phosphor: a systematic study of opto-electronic characteristics and thermal stability for lighting applications†

Pawan Kumar,[a] Devender Singh, *[a] Sitender Singh,[a] Harish Kumar[b] and Ramesh Kumar[c]

A series of green-emitting $Y_{2-x}Si_2O_7$:xEr^{3+} phosphors (x = 1–7 mol%) have been successfully synthesized using a straightforward gel-combustion method facilitated by urea. X-ray diffraction analysis provided specific patterns for samples, confirming a consistent triclinic phase across erbium-doped structures compared to undoped structures. Studies using TEM and EDX were conducted to identify the surface-related characteristics and chemical composition of the synthesized nanophosphor, respectively. The band gap was determined to be 5.55 eV and 5.80 eV for the host material and optimal sample, respectively. The primary peak of excitation, observed at 379 nm, represents the highly sensitive electric dipole transition from the $^4I_{15/2}$ state to the $^4G_{11/2}$ level, suggesting that the prepared phosphors could effectively absorb NUV light for activation. The PL profiles of $Y_{2-x}Si_2O_7$:xEr^{3+} (x = 1–7 mol%) phosphors demonstrate characteristic emissions at 409 nm ($^2H_{9/2} \rightarrow {}^4I_{15/2}$), 522 nm ($^2H_{11/2} \rightarrow {}^4I_{15/2}$), 553 nm ($^4S_{3/2} \rightarrow {}^4I_{15/2}$) and 662 nm ($^4F_{9/2} \rightarrow {}^4I_{15/2}$). In accordance with Dexter's theory, luminescence quenching observed at a concentration of 4 mol% Er^{3+} is attributed to dipole-quadrupole interactions. The optimal sample demonstrates excellent thermal stability, indicated by its luminescence at different temperatures and activation energy of 0.2641 eV. Additionally, the CIE, color purity and CCT values of the fabricated nanomaterials make it ideal for use in lighting applications.

Received 24th May 2024
Accepted 26th May 2024

DOI: 10.1039/d4ra03833a

rsc.li/rsc-advances

1 Introduction

Today, the rapid growth of the population and the swift pace of economic development have spurred a notable surge in energy demand, contributing significantly to the recent uptick in global carbon emissions.[1,2] Consequently, there has been a growing global interest in renewable energy sources and environmental preservation. Approximately 20% of the world's electricity consumption is attributed to lighting.[3] Presently, white light-emitting diodes (WLEDs) have garnered considerable attention as next-generation solid-state lighting to substitute conventional lamps[4,5] owing to their notable advantages, including high energy efficiency, extended operational lifespan, compactness and eco-friendliness.[6,7] The current mainstream commercial white LEDs utilize a combination of blue InGaN-LED-chips and YAG:Ce^{3+} yellow phosphors to produce white light.[8] This pairing generates white light through a blend of two-color emission bands. However, the resulting white light suffers from drawbacks such as a poor color-rendering-index (CRI <80) and high correlated color temperature (CCT >4500 K) because it lacks a red-emitting component.[9–11] This limitation restricts its suitability for indoor lighting applications. To address this issue and achieve white light with improved CRI and lower CCT values, an alternative approach has emerged. This method involves employing near-ultraviolet LED-chips to stimulate tricolor (RGB) phosphors.[12,13] At present, the wide color gamut WLED backlight is mainly composed of a blue InGaN chip, K_2SiF_6:Mn^{4+} red phosphor and green b-SiALON:Eu^{2+} phosphor.[14] However, the long decay time (~8 ms) of the K_2SiF_6:Mn^{4+} (KSF:Mn^{4+}) red phosphor easily affects the image-retention performance of fast-response backlight displays.[15] Apparently, the phosphor for LEDs should not only possess a broad excitation band appropriate to LED chip emission and narrow band emission with high color purity, but also have an appropriate decay time. For solid-state lighting, the commercial

[a]Department of Chemistry, Maharshi Dayanand University, Rohtak-124001, Haryana, India. E-mail: devjakhar@gmail.com
[b]Department of Chemistry, School of Chemical Sciences, Central University of Haryana, Mahendergarh-123031, India
[c]Department of Chemistry, Kurukshetra University, Kurukshetra-136119, Haryana, India

† Electronic supplementary information (ESI) available. See DOI: https://doi.org/10.1039/d4ra03833a

WLED is a phosphor-converted light-emitting diode (LED) fabricated by a combination of an InGaN chip and YAG:Ce^{3+} phosphor. However, due to the lack of a red component, this type of WLED exhibits a cold white light emission with low color-rendering index (CRI <80) and high correlated color temperature (CCT >4500 K). It is thus clear that red phosphor is an important part of assembling high-CRI light sources. Presently, non-rare-earth Mn^{4+} red phosphors have been used in the packaging of WLEDs due to their high luminous efficacy and low cost.[16] These phosphors possess unique properties such as exceptional thermal and chemical stability, cost-effectiveness, straightforward synthesis techniques and outstanding optical characteristics, resulting in significantly enhanced luminescence emission.[17–19] Within the lanthanide series, erbium (Er^{3+}) stands out for its ability to generate intense green emissions through down-conversion photoluminescence. This phenomenon arises from transitions such as $^2H_{9/2} \rightarrow {}^4I_{15/2}$, $^2H_{11/2} \rightarrow {}^4I_{15/2}$, $^4S_{3/2} \rightarrow {}^4I_{15/2}$, and $^4F_{9/2} \rightarrow {}^4I_{15/2}$.[20,21] In addition to the activators, the choice of the host material holds significant importance as it can impact the photoluminescence (PL) properties of the dopant ions. Factors such as the crystal field strength, covalent nature, and potential energy transfer between the host and dopant ions all play roles in influencing these properties.[22,23] The host lattice $Y_2Si_2O_7$ is known for its exceptional thermal and chemical stability. It exhibits complex high-temperature polymorphism, existing in various structural phases denoted as α, β, γ, δ, γ, and η forms.[24] Among these, α-$Y_2Si_2O_7$ is characterized as a low-temperature phase and crystallizes into a triclinic structure with a $P\bar{1}$ space group.[25]

However, a significant challenge lies in preparing this system as a single-phase material. Achieving a homogeneous, single-phase material is essential for many applications, and overcoming this challenge often requires precise control over the synthesis conditions and processing techniques. It is essential to establish direct synthetic routes for fabricating Er^{3+}-doped $Y_2Si_2O_7$ luminescent nanoparticles, allowing precise manipulation of their crystalline phase, morphology and dimensions. This control enables customization of their optical characteristics, opening avenues for applications in multiple domains. As a result, several chemical techniques, such as sol–gel, chemical vapor deposition and microwave-assisted methods, have been developed to address this requirement.[26–28] Among these techniques, this study focuses on the gel-combustion method due to its distinct advantages. These methods offer several advantages, including simplicity in synthesis, capability to produce nano-sized crystalline powders with high purity at low temperatures, and improved homogeneity.[29,30] These characteristics make the gel-combustion method particularly well-suited for the production of Er^{3+}-doped $Y_2Si_2O_7$ nanoparticles with tailored properties for a range of applications. In this study, $Y_2Si_2O_7$:Er^{3+} phosphors containing different amounts of Er^{3+} were produced using an auto gel-combustion approach. To the author's knowledge, there are no existing reports on the synthesis of $Y_2Si_2O_7$ doped with Er^{3+} ions using this combustion method. The research thoroughly examined various properties, including diffraction, morphology, chemical composition, band gap, photoluminescence, thermal luminescence quenching and photometric characteristics.

2 Experimental

2.1 Synthesis and instrumentations

The gel combustion approach was utilized to produce Er^{3+}-activated $Y_2Si_2O_7$ nanophosphors. The initial ingredients are greatly purified A.R. grade compounds with a purity of 99.99% of the metal nitrates groups, *i.e.*, yttrium nitrate, erbium nitrate,

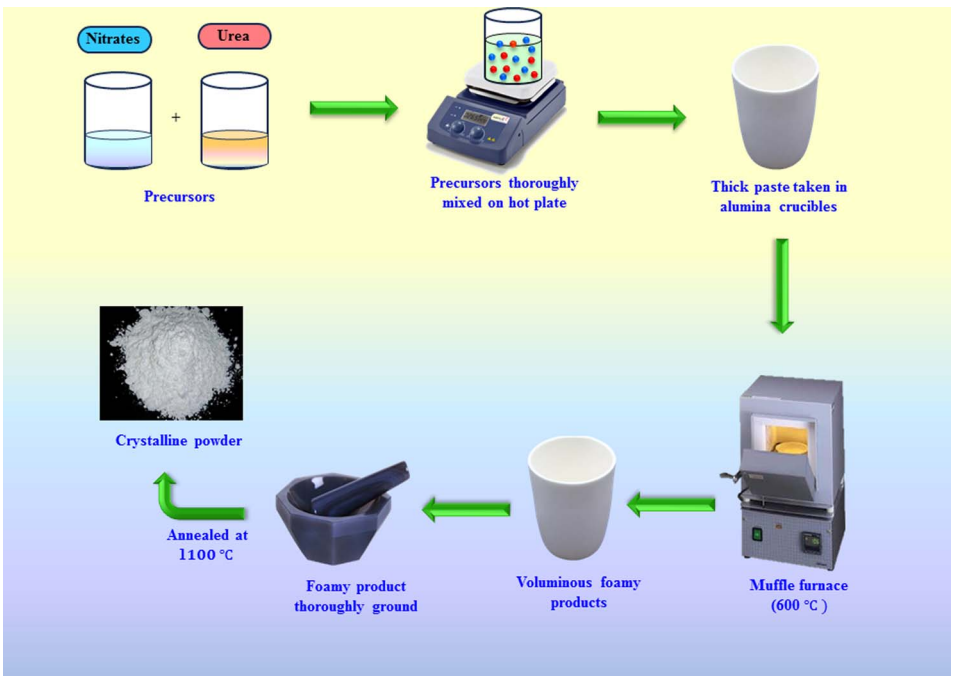

Fig. 1 Synthetic diagram of the gel-combustion process.

silica, nitric acid and urea were procured and used without any further purification. Metal nitrate precursors were utilized due to their low disintegration temperature. Combustion was facilitated by low-temperature deterioration and the solubility of metallic precursors in water. Oxygen was generated as nitrates disintegrated, while urea acted as a fuel. Various compositions of Er^{3+} (1–7 mol%) were incorporated into the YPS lattice. A stoichiometric mixture of metal nitrites was heated to form a gel solution, which was then heated further with urea and water. Combustion occurred at 600 °C, producing gases (N_2, CO_2 *etc*) and porous flaky nanophosphors. The process released significant energy, resulting in a crystalline structure and reduced particle size.[31] The synthesized materials were then calcined at 1100 °C for three hours to achieve the desired phase. Fig. 1 depicts the illustrated explanation of the combustion synthesis method. Powder X-ray diffraction analysis was conducted using a Rigaku Ultima X-ray diffractometer, operating at 40 kV and 40 mA with Cu-Kα radiation, to confirm the crystal structure and phase purity of the prepared phosphors. Diffuse reflection spectra of the samples were obtained using an integrated sphere-mounted UV-vis-NIR spectrophotometer (UV-3600, SHIMADZU). The morphology of the doped nanopowders was examined using a transmission electron microscope (JEOL JEM-1400 Plus). Energy dispersive X-ray (EDX) analysis was performed using a Hitachi SU-8010 SERIES. Moreover, the photoluminescence (PL) and photoluminescence excitation (PLE) spectra of the samples were examined using a spectrophotometer (Fluorolog-3-Horiba) outfitted with a 150 W xenon lamp.

3 Results and discussion

3.1 XRD evaluation

X-ray diffraction (XRD) patterns for $Y_2Si_2O_7$ (YPS) and its variants doped with different concentrations (1–7 mol%) of Er^{3+} ions, spanning a scan range of 10° to 80°, are depicted in Fig. 2(a). These patterns correspond closely with the established disilicate structure of $Y_2Si_2O_7$, as described by JCPDS card no. 38-0223, which is characterized by a triclinic phase with space group $P\bar{1}$.[32] No additional peaks appeared in the patterns after introducing Er^{3+} ions, indicating the maintenance of a single phase in the material. Fig. 2(b) shows that the XRD peaks shift for the samples containing Er^{3+}; as the concentration of Er^{3+} in the undoped $Y_2Si_2O_7$ increases, the peaks shift towards lower angles. This shift is attributed to the smaller ionic radius of Er^{3+} compared to Y^{3+} within the same coordination environment. When smaller Er^{3+} ions replace larger Y^{3+} ions in the structure, the inter-planar distances diminish. This reduction leads to an increase in the diffraction angles, which aligns with Bragg's equation, "$2d \sin\theta = n\lambda$".[33] In this equation, "n" represents an integer, d symbolizes the inter-planar distance, θ is the diffraction angle and λ is the wavelength of the X-rays. This adjustment in the inter-planar spacing and the corresponding shift in diffraction angles can be directly linked to the substitution of the ion sizes within the crystal lattice. This observation confirms that the Er^{3+} ions have been successfully incorporated

Table 1 Determined interplanar d-spacing values of the host and Er^{3+}-doped phosphors

Sample	2θ-Angle	d-Spacing (Å)
$Y_2Si_2O_7$ (YPS)	29.32	3.0437
YPS:1 mol% Er^{3+}	29.33	3.0427
YPS:2 mol% Er^{3+}	29.35	3.0406
YPS:3 mol% Er^{3+}	29.36	3.0396
YPS:4 mol% Er^{3+}	29.39	3.0366
YPS:5 mol% Er^{3+}	29.43	3.0325
YPS:6 mol% Er^{3+}	29.45	3.0305
YPS:7 mol% Er^{3+}	29.47	3.0285

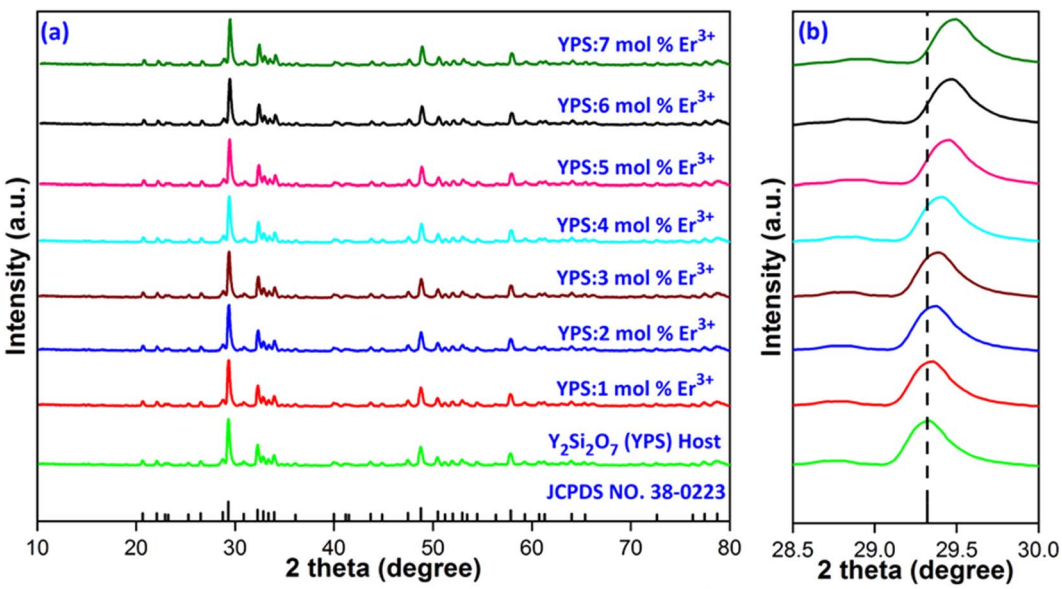

Fig. 2 (a) Diffraction patterns of $Y_2Si_2O_7$ and $Y_{2-x}Si_2O_7$:xEr^{3+} (x = 1–7 mol%) phosphors. (b) Enlarged pattern view of all considered samples.

into the Y^{3+} ion sites within the YPS matrix. The shift in the diffraction angles and the reduction of the inter-planar distances provide clear evidence of the substitution, indicating that the doping process was effective (Table 1). Eqn (1) assesses the percentage difference in the radius (D_r) between the doped ion and substituted cation within the host, serving to verify this substitution. This equation quantifies the alteration in ionic radii, offering a precise method to confirm the successful inclusion of Er^{3+} ions into Y^{3+} sites within YPS host.[34]

$$D_r = \frac{R_h(CN) - R_d(CN)}{R_h(CN)} \times 100\% \quad (1)$$

In the mentioned equation, R_h(CN) and R_d(CN) represent the ionic-radii and coordination numbers of the host and entering (doped) cation, respectively. The equation helps to determine whether the size difference between the host ion and the doped ion is within an acceptable limit, which typically should not exceed 30%. The calculated value, being within this range, supports the successful incorporation of the doped ion into the host matrix. In this case, it further confirms the effective doping of Er^{3+} ions into the host matrix, indicating that the radii of Er^{3+} and substituted ion are sufficiently close to allow for effective substitution without disrupting the crystal lattice. Scherrer's equation was employed to determine the crystallite size (D) of samples containing varying concentrations of activated ions. This eqn (2) is pivotal in the analysis of X-ray diffraction data to estimate the size of crystallites, taking into account the broadening of diffraction peaks due to particle size effects.[35]

$$D_{hkl} = \frac{k\lambda}{\beta(2\theta)\cos\theta} \quad (2)$$

In this equation, λ represents the X-ray wavelength, (0.154 nm for Cu Kα radiation) and β is the full width at half maximum of the diffraction peak. The shape factor (k), referred to as the Scherrer constant with a value of 0.89, is dimensionless and accounts for the shape of the crystallite assumed in the calculation. Table 2 provides a comprehensive overview of the crystallite size, which varies across different samples with varying concentrations of activated ions. When examining X-ray line-widening in samples, both crystallite size and strain contribute to the effect. The Williamson–Hall (W–H) plot offers a method to collectively analyze these contributions. In accordance with the W–H relation, the total width at half maximum (β) is defined as a linear amalgamation of contributions originating from the size of the crystallites (D) and level of strain (ε). The pertinent equation is presented below.[36]

Table 2 Computed diffraction values of $Y_2Si_2O_7$ and $Y_{2-x}Si_2O_7$:xEr^{3+} (x = 1–7 mol%) phosphors

Sample (YPS)	2 theta (2θ)	FWHM	Crystallite size (nm) Scherrer's	W–H	Microstrain ($\varepsilon \times 10^{-4}$)
$Y_2Si_2O_7$ (YPS)	29.32	0.2997	27.40	35.58	5.1421
YPS:1 mol% Er^{3+}	29.33	0.3037	27.30	34.19	5.3012
YPS:2 mol% Er^{3+}	29.35	0.3152	26.07	33.43	5.6017
YPS:3 mol% Er^{3+}	29.36	0.3310	24.83	32.59	5.9271
YPS:4 mol% Er^{3+}	29.39	0.3374	24.35	31.19	6.1724
YPS:5 mol% Er^{3+}	29.43	0.3419	24.31	29.34	6.4587
YPS:6 mol% Er^{3+}	29.45	0.3774	24.05	27.71	6.7410
YPS:7 mol% Er^{3+}	29.47	0.3807	20.86	26.48	7.0241

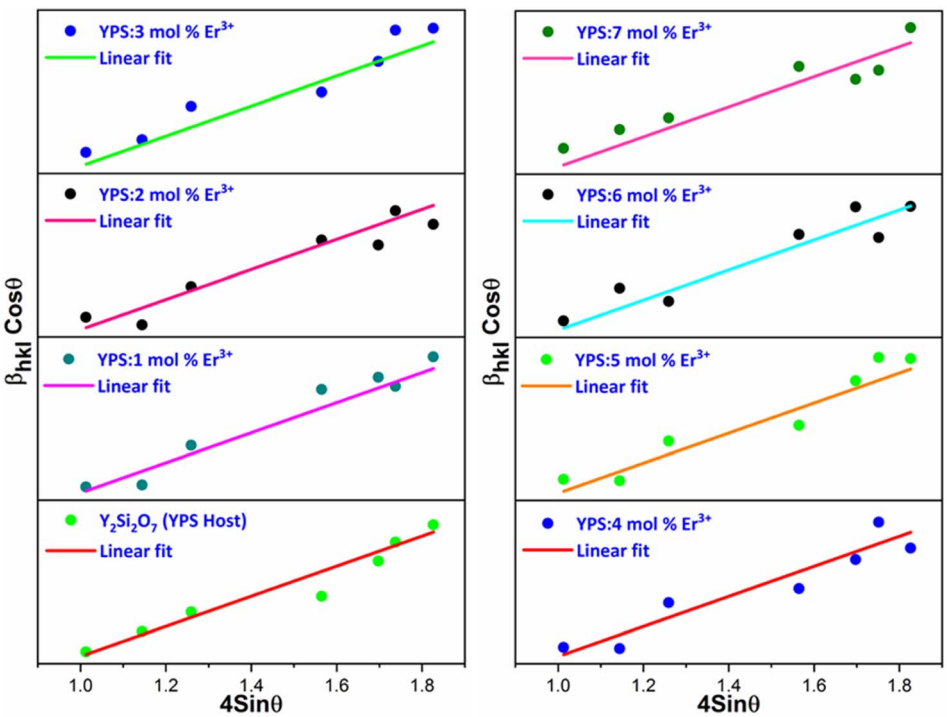

Fig. 3 W–H plot of $Y_2Si_2O_7$ and various doped $Y_{2-x}Si_2O_7$:xEr^{3+} (x = 1–7 mol%) phosphors.

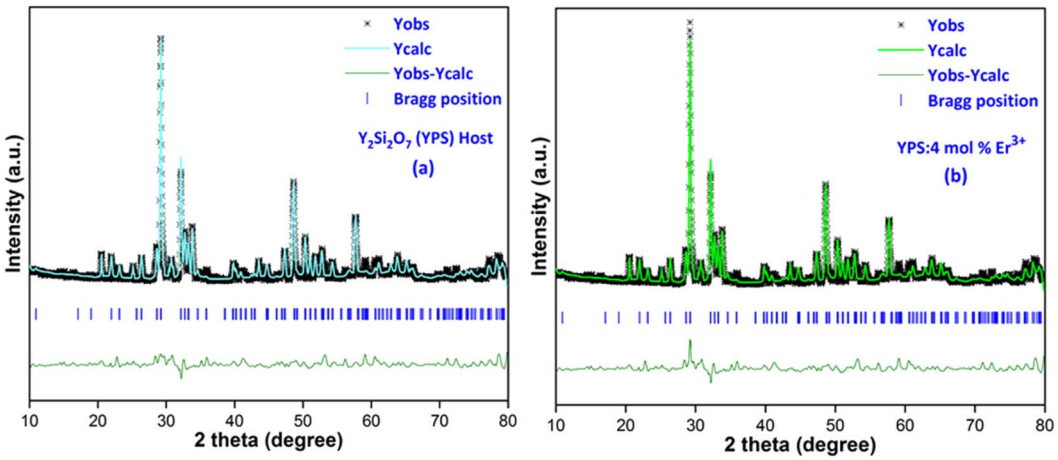

Fig. 4 Rietveld profiles of the (a) $Y_2Si_2O_7$ and (b) $Y_{1.96}Si_2O_7$:4 mol% Er^{3+} phosphor.

$$\beta_{hkl} \cos \theta_{hkl} = \frac{K\lambda}{D} + 4\varepsilon \sin \theta_{hkl} \quad (3)$$

This expression allows for the determination of both crystallite size and strain from the X-ray diffraction data. In the given straight-line formula, a linear relationship between 4 sin θ (on the x-axis) and $\beta \cos \theta$ (on the y-axis) is depicted. The intercept is used to derive the values of the crystallite size, while the slope of the line is employed to compute the value of the strain. Fig. 3 presents the Williamson–Hall visualizations of the host and all doped YPS:xEr^{3+} (x = 1–7 mol%) nanomaterials. This figure likely offers a graphical representation of how the crystallite size and strain vary across different samples, providing valuable insights into the structural characteristics of the doped materials compared to the host material. The Rietveld refinement method assesses the intensity profile, providing a reliable model for the crystal properties. Fig. 4(a & b) shows the Rietveld profiles for YPS and YPS doped with 4 mol% Er^{3+} nanophosphor. All refined data align with the initial model, with reliability factors within a sufficient range. Table 3 outlines the refinement details, indicating that all samples belong to the triclinic system with space group P$\bar{1}$. Crystallographic parameters decrease from the host material to the optimized sample, indicating effective Er^{3+} inclusion.

Table 3 Refinement outcomes of $Y_2Si_2O_7$ (YPS) and YPS:4 mol% Er^{3+} phosphors

Sample	$Y_2Si_2O_7$ (YPS)	YPS:4 mol% Er^{3+}
2θ range; step (deg.)	10–80; 0.02	10–80; 0.02
System	Triclinic	Triclinic
Lattice-type	P	P
Wavelength (Å)	1.541	1.541
Space group	$P\bar{1}$	$P\bar{1}$
Space group number	2	2
Formula unit (N)	4	4
α	97.23	97.20
β	89.80	89.76
γ	87.50	87.43
a (Å)	6.556	6.507
b (Å)	6.759	6.578
c (Å)	12.274	11.7721
Volume (Å^3)	539.03	499.381
χ^2	3.14	3.72
R_p (%)	5.77	6.11
R_{wp} (%)	7.59	8.41

3.2 TEM and EDX analyses

The TEM image is used to analyze the sample structure, framework and crystal size. Fig. 5 shows the TEM picture of the optimal sample, revealing the uniformly spread and roughly spherical particles ranging from 25–45 nm. Minor discrepancies in crystallite size were due to uneven heat and mass flow during combustion.[37] In Fig. 6(a and b), EDX plots of the $Y_2Si_2O_7$ (YPS) host and 4 mol% Er^{3+}-doped YPS nanophosphor are shown. Fig. 6(a) displays the peaks for Y, Si and O, while Fig. 6(b) shows the peaks for Y, Si, O and Er, confirming their chemical compositions. The presence of Er peaks confirms uniform doping. Table of insets listed the elemental

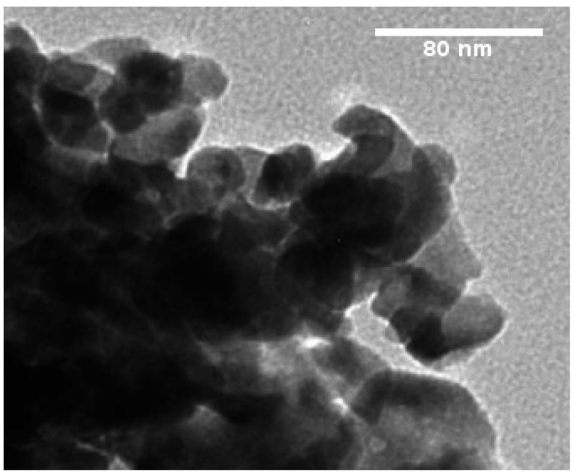

Fig. 5 TEM image of the YPS:4 mol% Er^{3+} nanophosphor.

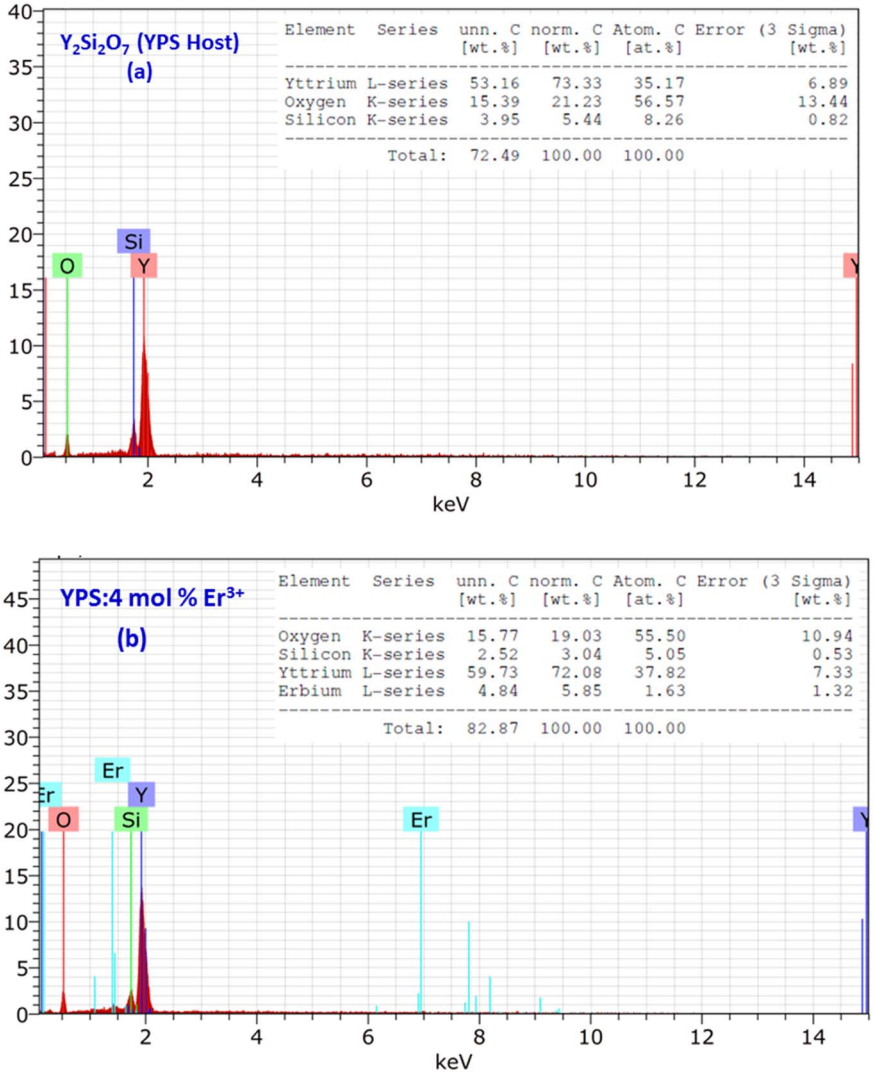

Fig. 6 EDX profiles of (a) the $Y_2Si_2O_7$ and (b) $Y_{1.96}Si_2O_7$:4 mol% Er^{3+} phosphor. The inset represents the chemical composition of the respective samples.

compositions of both samples. No additional emissions indicate the formation of pure $Y_2Si_2O_7$ and $Y_2Si_2O_7$:Er^{3+} phosphors, supporting the PL and XRD results.

3.3 Photoluminescence study

3.3.1 Excitation and emission spectra. To explore the light emission performance of the fabricated phosphors, their excitation (PLE) spectra were examined within the 200–550 nm wavelength range, at an emission of 550 nm for Er^{3+}. Fig. 7 illustrates the PLE spectra of the YPS phosphors with 4 mol% doping concentration of Er^{3+}, showcasing prominent peaks at ~350 nm ($^4I_{15/2} \rightarrow {}^4G_{7/2}$), ~366 nm ($^4I_{15/2} \rightarrow {}^4G_{9/2}$), ~378 nm ($^4I_{15/2} \rightarrow {}^4G_{11/2}$), ~408 nm ($^4I_{15/2} \rightarrow {}^2G_{9/2}$), ~450 nm ($^4I_{15/2} \rightarrow {}^4F_{5/2}$), ~489 nm ($^4I_{15/2} \rightarrow {}^4F_{7/2}$), and ~523 nm ($^4I_{15/2} \rightarrow {}^2H_{11/2}$).[38,39] Additionally, a broad-band spanning 230–330 nm is observed, indicating the charge transfer band (CTB) from O^{2-} to Er^{3+}. The highest peak, occurring at 378 nm, resembles the $^4I_{15/2} \rightarrow {}^4G_{11/2}$ transition of erbium ions. This finding suggests that the phosphor under study could potentially be used in the production of near-ultraviolet light emitting diodes (NUV-LEDs). The photoluminescence (PL) emission spectra (Fig. 8) of YPS:$x$$Er^{3+}$ (x = 1–7 mol%) phosphors display prominent peaks at ~409 nm, ~523 nm, ~549 nm and ~673 nm, indicating the $^2H_{9/2} \rightarrow {}^4I_{15/2}$, $^2H_{11/2} \rightarrow {}^4I_{15/2}$, $^4S_{3/2} \rightarrow {}^4I_{15/2}$ and $^4F_{9/2} \rightarrow {}^4I_{15/2}$ transitions, respectively.[40,41] Among these, the strong green emission at 553 nm, resulting from the $^4S_{3/2} \rightarrow {}^4I_{15/2}$ transition, stands out because of the electric dipole (ED) nature ($\Delta J = 3$).

3.3.2 Concentration quenching (CQ). The emission intensities increased gradually until they peaked with a concentration of Er^{3+} ions ranging from 1 to 4 mol%. Subsequently, the luminous intensity decreased due to CQ, as illustrated in Fig. 9. The process of concentration quenching may involve non-radiative energy transfer among the Er^{3+} ions. Non-radiative energy transfer among erbium ions (Er^{3+}), which is often attributed to exchange interaction, radiation re-absorption and multipolar interaction, can lead to concentration quenching. Initially, the PL intensity rises with the Er^{3+} doping

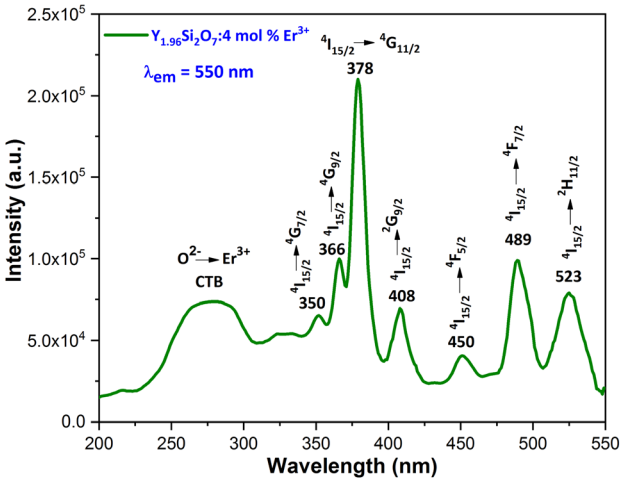

Fig. 7 Excitation spectrum of the $Y_{1.96}Si_2O_7$:4 mol% Er^{3+} nanophosphor.

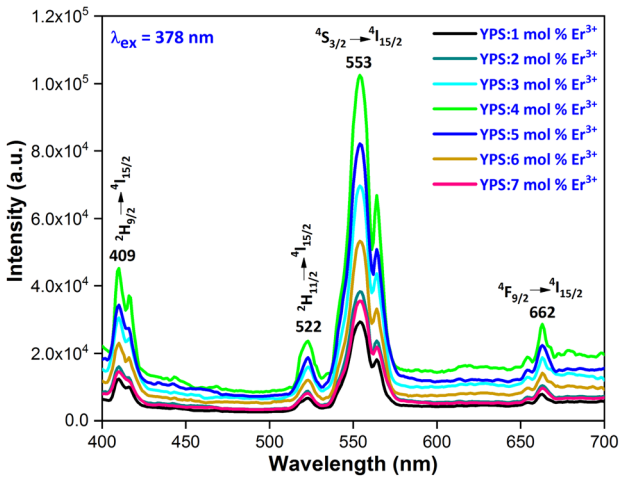

Fig. 8 Emission spectrum of the $Y_{2-x}Si_2O_7$:xEr^{3+} (x = 1–7 mol%) nanophosphors.

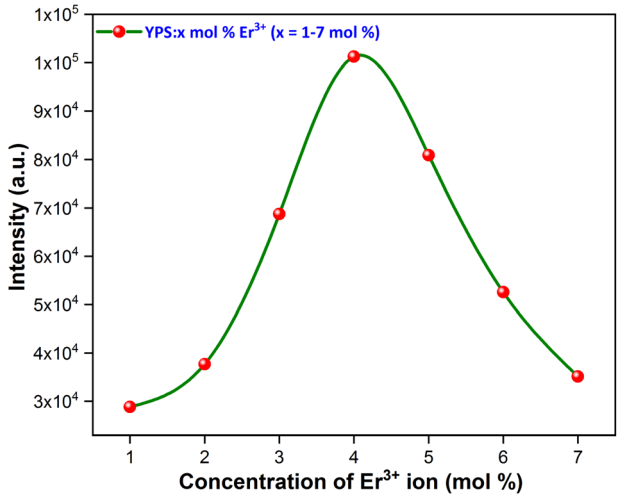

Fig. 9 Concentration quenching profile of the considered nanophosphors.

concentration, but decreases beyond a critical concentration (x_c). At this point, the critical distance (R_c) between ions is reduced enough to enable energy transfer. Blasse's eqn (4) is used to approximate the critical distance between activators.[42]

$$R_c = 2\left(\frac{3V}{4\pi x_c N}\right)^{1/3} \quad (4)$$

In this context, "x_c" represents the ideal concentration, "V" stands for volume and "N" denotes the cation count within the unit cell. In the current investigation, these variables are determined as $x_c = 0.04$, V = 499.381 Å^3 and $N = 4$. The critical distance for energy transfer is estimated at about 18.162 Å. Typically, when the value of "R_c" is around 5 Å, the exchange-interaction becomes the driving force behind energy transfer. The energy transfer among Er^{3+} ions in the YPS:Er^{3+} phosphor, with R_c exceeding 5 Å, likely occurs through multipolar interactions, such as dipole–dipole, dipole–quadrupole, and quadrupole–quadrupole mechanisms. Dexter's theory states that when the same activator ions interact multipolarly, eqn (5) can determine the specific interaction causing concentration quenching in the phosphor.

$$\frac{I}{x} = k\left[1 + \beta x^{Q/3}\right]^{-1} \quad (5)$$

In this equation, Q represents the constant of the multipolar-interaction, taking values of 6, 8 and 10 for dipole–dipole (d–d), dipole–quadrupole (d–q) and quadrupole–quadrupole (q–q) interactions, respectively.[43] Meanwhile, k and β denote constants specific to the host material under the same excitation conditions. Eqn (6) can also be simplified as:

$$\log\left(\frac{I}{x}\right) = k - \frac{Q}{3}\log(x) \quad (6)$$

Eqn (6) was employed to generate a plot illustrating the correlation between log(x) and log(I/x), as depicted in Fig. 10.

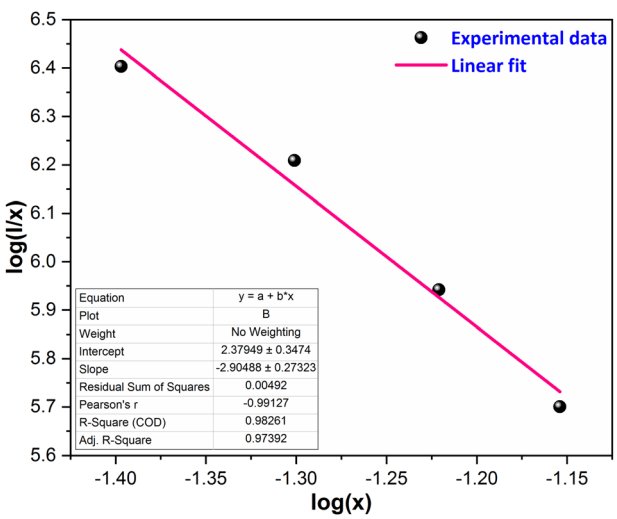

Fig. 10 Straight line-fitted graph between log(x) and log(I/x).

The data points on the graph were subjected to linear fitting, resulting in a slope of −2.90. Consequently, the calculated value of Q is approximately 8.7, which is assumed to be 8. This suggests that the dipole–quadrupole (d–q) interaction is probably accountable for the energy transfer among the dopant ions, thereby causing concentration quenching.

3.4 Luminescence lifetime

Fig. 11 illustrates the decay behavior of the YPS nanophosphor containing 4 mol% of erbium ions. The lifetime curve, obtained under excitation at 349 nm and emission at 578 nm, was analyzed using a bi-exponential decay function.[44]

$$I_t = I_0 + A_1 \exp(-t/\tau_1) + A_2 \exp(-t/\tau_2) \quad (7)$$

here, I and I_0 denote the luminescence intensities at time t and 0, respectively. τ_1 and τ_2 correspond to lifetime values for the fast and slow exponential components, respectively. Additionally, A_1 and A_2 are constants associated with the parameters for curve fitting. The formula used to determine the average lifetime for the fabricated phosphor is:

$$\tau_{avg} = (A_1 t_1^2 + A_2 t_2^2)/(A_1 t_1 + A_2 t_2) \quad (8)$$

The average lifetime achieved from the fitted results for YPS doped with various concentrations of Er^{3+} is as follows: 4.3492 ms for 1 mol%, 4.2024 ms for 2 mol%, 4.1021 ms for 3 mol%, 3.8192 ms for 4 mol%, 3.5034 ms for 5 mol%, 3.2110 ms for 6 mol%, and 2.9420 ms for 7 mol%. Fig. 12 shows Auzel's model, described by eqn (9), which was used to analyze the gradual decrease in lifetime values with increasing dopant concentration.

$$\tau_c = \tau_0 / 1 + \frac{C}{C_0} e^{-N/3} \quad (9)$$

In this context, "N" represents the phonon number involved in quenching *via* the cascade multi-phonon process, "C_o" is a constant, "τ_c" is the lifetime at concentration "C" and "τ_o" signifies the intrinsic lifetime. The intrinsic lifetime was determined to be 4.86 ms. The non-radiative relaxation rate (A_{nR}) is also calculated using the radiative-lifetime (τ_o) and average lifetime (τ_{avg}) in the following eqn (10).[45]

$$\frac{1}{\tau_{avg}} = \frac{1}{\tau_0} + A_{nR} \quad (10)$$

Quantum efficiency (η) is one of the significant parameters to describe the efficiency of the rare earth (RE)-doped material, and it was defined as the ratio between the light intensity emitted to the light intensity absorbed, and also described as a ratio of the experimental lifetime (τ_{avg}) and radiative lifetime (τ_o), as shown in the following eqn (11).

$$\eta_{int} = \frac{A_R}{A_R + A_{NR}} = \frac{\tau_{avg}}{\tau_0} \quad (11)$$

Quinine bisulphate was used as a reference to estimate the value of the extrinsic quantum efficiency *via* eqn (12).[46]

$$\eta_{ext} = \frac{\eta_r A_r I_s n_s^2}{A_s I_r n_r^2} \quad (12)$$

here, η_s is the quantum efficiency of the sample; η_r represents the quantum efficiency of the reference, A is the absorbance at the excitation wavelength, and I is used for the integrated emission intensity. Also, s, r and n are used for the refractive index of the sample, reference and solvent, respectively. Table 4 lists the lifetime, non-radiative transition rate, intrinsic quantum efficiency and extrinsic quantum efficiency values of the synthesized nanophosphors.

3.5 Optical band gap analysis

The optical band-gap of a material is pivotal in optoelectronic applications. In the case of the prepared phosphors, this

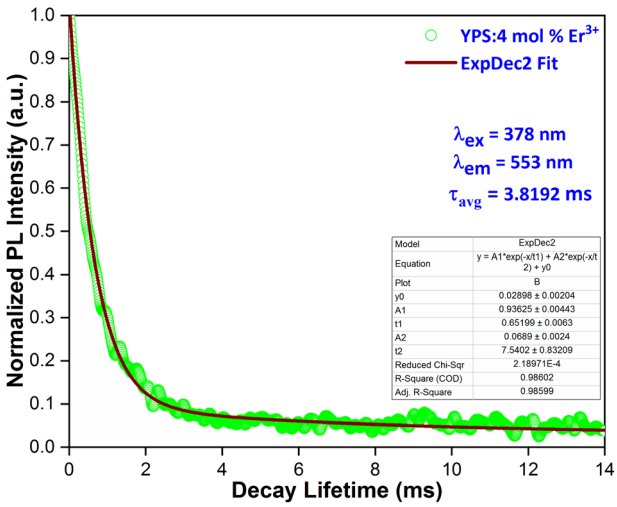

Fig. 11 Lifetime curve of the $Y_{1.96}Si_2O_7$:4 mol% Er^{3+} nanophosphor.

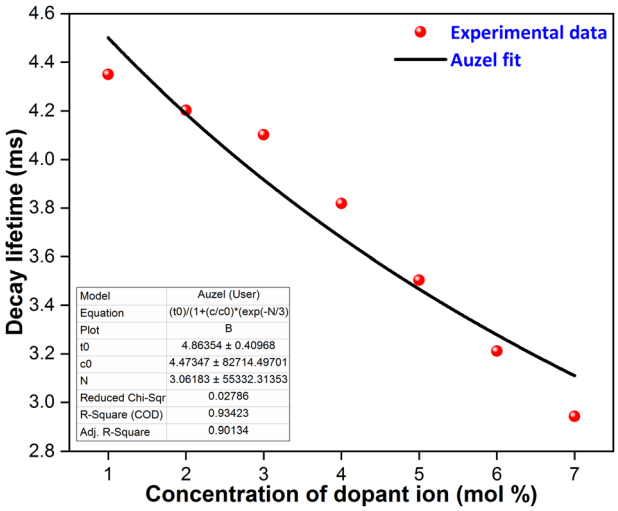

Fig. 12 Auzel's fitting curve of $Y_{2-x}Si_2O_7$:xEr^{3+} (x = 1–7 mol%) phosphors.

Table 4 Decay time and quantum efficiency of $Y_{2-x}Si_2O_7$:xEr^{3+} ($x = 1$–7 mol%) phosphors

Sample	τ_{avg} (ms)	A_{nR} (S^{-1})	(η_{int}%)	(η_{ext}%)
YPS:1 mol% Er^{3+}	4.3492	24.22	89.48	19
YPS:2 mol% Er^{3+}	4.2124	31.69	86.67	17
YPS:3 mol% Er^{3+}	4.1021	38.08	84.40	14
YPS:4 mol% Er^{3+}	3.8192	56.13	78.58	11
YPS:5 mol% Er^{3+}	3.5034	79.73	72.08	10
YPS:6 mol% Er^{3+}	3.2110	105.72	66.07	8
YPS:7 mol% Er^{3+}	2.9420	134.20	60.53	6

parameter has been determined through diffuse reflectance spectroscopy (DRS). This method deals with the decline in incident light after it is absorbed or reflected by the surface of the matrix. For powder samples, dispersion occurs extensively, making it challenging to measure the scattered intensity ideally. Therefore, the reflectance mode is optimal for accurately measuring this parameter. Fig. 13 depicts the DRS of $Y_2Si_2O_7$ (YPS) and YPS:4 mol% Er^{3+} in the 200–800 nm range. Charge transfer between O^{2-} and Er^{3+} is represented by the band at 245–275 nm in the doped sample. Additional peaks at 378 nm, 489 nm, and 523 nm are ascribed to the $^4I_{15/2} \rightarrow {}^4G_{11/2}$, $^4I_{15/2} \rightarrow {}^4F_{7/2}$, and $^4I_{15/2} \rightarrow {}^4H_{11/2}$ transitions of Er^{3+}, respectively. The obtained DRS data were transformed into absorption using the Kubelka–Munk (KM) function, as described below.[47]

$$F(R) = \frac{K}{S} = \frac{(1-R)^2}{2R} \quad (13)$$

here, R defines the ratio of the focused phosphor's reflectance to that of the reference, and $F(R)$ defines the KM function. The absorptions and scattering coefficients are denoted by K and S, respectively. Using Tauc's eqn (14), the band-gap was computed and is shown below.

$$\alpha h\nu = C(h\nu - E_g)^n \quad (14)$$

here, C, $h\nu$ and E_g stand for the constant, energy of the incident light, and the optical band-gap, respectively. Here, n equals $\frac{1}{2}$, indicative of the direct band-gap for the focused nanomaterials. When the material is subjected to a 60-degree angle of exposure, the interplay of the aforementioned equations, under this specific condition, leads to $K = 2\alpha$ and S functions as a constant, giving rise to an additional expression.[48]

$$[F(R)h\nu]^2 = C(h\nu - E_g) \quad (15)$$

The band-gap value was determined by projecting the curve onto $[F(R)h\nu]^2 = 0$ in the graphical representation of $[F(R)h\nu]^2$ *versus* $h\nu$. The calculated band-gap values are 5.55 eV for the host and 5.80 eV for the phosphor doped with 4 mol% Er^{3+}, as illustrated in Fig. 14. The fluctuations in the optical band gap observed in both pure and doped samples could be attributed to the level of structural disorder present in the host matrix.

3.6 Temperature-dependent luminescence and activation energy

The thermal stability of materials is a crucial aspect for their application in phosphor-converted LEDs, especially since high-power LED chips are typically used in environments with elevated temperatures. Due to the effect known as thermal quenching, a phosphor's luminescence tends to diminish when its temperature is increased beyond ambient levels. However, for a phosphor material to be considered viable for real-world white LED (WLED) applications, it must maintain its conversion efficiency even at temperatures up to 423 K. This requirement is because the temperature of a nanophosphor layer can rise to match the LED's junction temperature, which generally occurs in the 373–423 K range.[49] Fig. 15(a) shows how the luminescence spectra of $Y_2Si_2O_7$ doped with 4 mol% Er^{3+} changes with temperature, ranging from 298 K to 498 K, under a 378 nm excitation. The data indicate a steady decrease in the luminescence intensity as the temperature increases. Fig. 15(b)

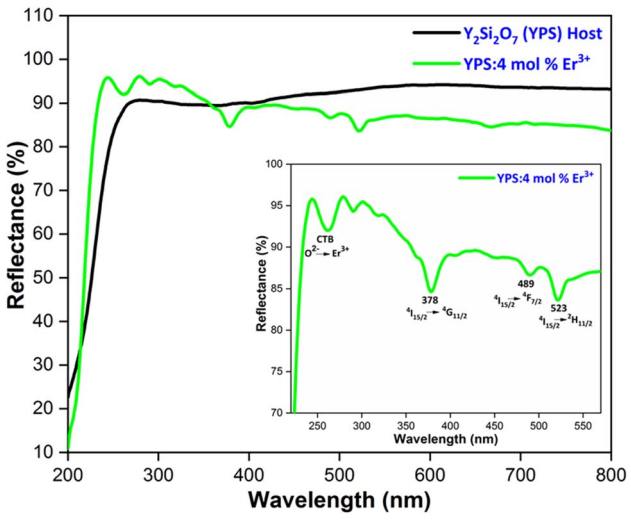

Fig. 13 DRS spectra of the host and $Y_{1.96}Si_2O_7$:4 mol% Er^{3+} nanophosphor.

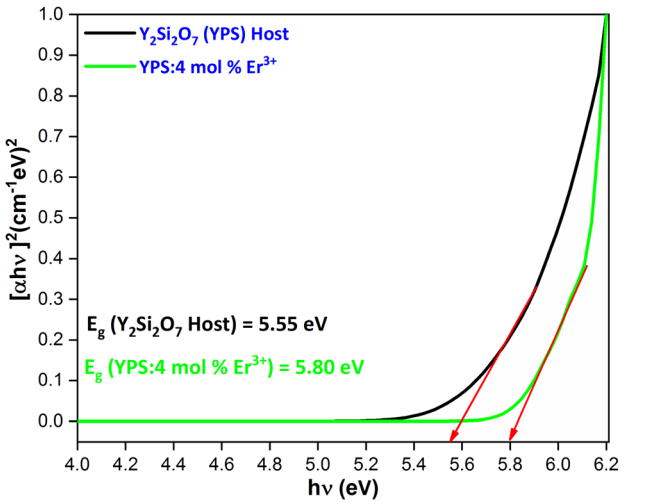

Fig. 14 for the $Y_2Si_2O_7$ and $Y_{1.96}Si_2O_7$:4 mol% Er^{3+} phosphor.

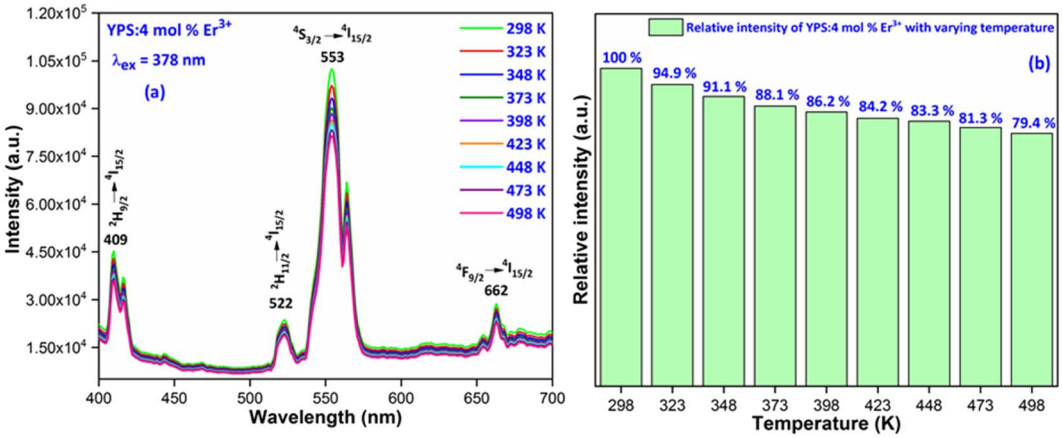

Fig. 15 (a) Temperature-dependent photoluminescence and (b) relative emission intensity with varying temperature of the $Y_{1.96}Si_2O_7$:4 mol% Er^{3+} phosphor.

details this reduction in emission intensity as the temperature rises, demonstrating a consistent decline attributed to the thermal quenching effect. Interestingly, the luminous intensity at 423 K remains at 84.2% of its original intensity at 298 K, suggesting that this synthesized sample is promising for use in white LED (wLED) applications. To gain deeper insight into the thermal-quenching behavior observed in the prepared material, the activation energy was calculated employing a specific formula (16). This calculation is essential for quantifying the energy barrier that electrons must overcome during thermal quenching, providing insights into the material's thermal stability and its performance in a high-temperature environment.

$$I_T = \frac{I_0}{1 + A\exp\left(-\frac{E_a}{kT}\right)} \tag{16}$$

here, k is the Boltzmann's constant (8.617105×10^{-5} eV K^{-1}), A is a constant; and I_T and I_0 stand for the luminous intensity at the target temperature and room temperature, separately. E_a is the activation energy needed for thermal quenching. In general, greater thermal stability exists when the E_a value is higher. Thus, the dependency of $\ln[(I_0/I_T) - 1)]$ on $1/kT$ may be expressed as.[50]

$$\ln\left(\frac{I_0}{I_T} - 1\right) = \ln A - \frac{E_a}{kT} \tag{17}$$

This relationship is illustrated in Fig. 16, where the activation energy for the phosphor is calculated to be approximately 0.2641 eV, derived from the slope of the linear fit to the data plotted on the graph. In this case, the relatively high activation energy suggests that the phosphor possesses good thermal stability, enabling it to maintain performance at higher temperatures.

3.7 Photometric investigation

The color emission characteristics of the YPS:xEr^{3+} samples (x = 1–7 mol%) were analyzed, resulting in color points plotted on

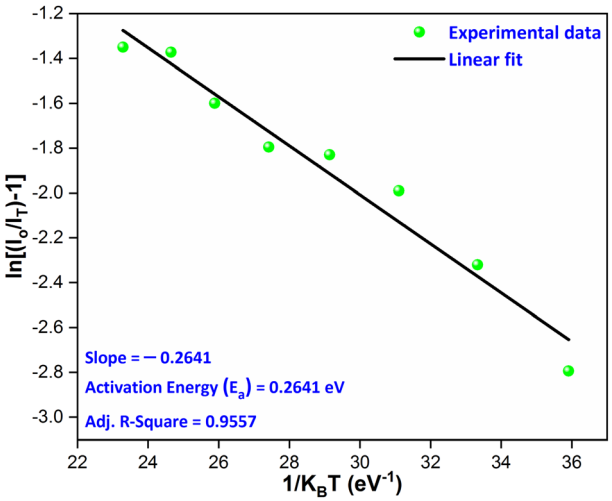

Fig. 16 Linear fitted graph for the calculation of the activation energy.

CIE charts (Figs. S1–S7†). These coordinates (Table 5) consistently fall within the green region, confirming the uniform color output. The green emission coordinates adhere to the criteria set by both the European Broadcasting Union and the National Television System Committee, making these materials suitable for incorporation into the green segment of RGB-based white LEDs. Table 5 elaborates the color purity, which can be computed *via* the following formula.[51]

$$\mathrm{CP} = \sqrt{\frac{(x - x_i)^2 + (y - y_i)^2}{(x_d - x_i)^2 + (y_d - y_i)^2}} \times 100 \tag{18}$$

The equation calculates the color purity using the coordinates (x, y) of the current synthesized nanomaterials, ideal-white-light (x_i, y_i), and dominant wavelength (x_d, y_d). The highest achieved purity is 87.23% for the optimum sample. The analysis characterizes green emission by determining the correlated color temperature (CCT) using the McCamy formula. This calculation offers a comprehensive insight into the nature (warm or cool) of emitted light.[52]

Table 5 Chromaticity parameters of $Y_{2-x}Si_2O_7$:xEr^{3+} (x = 1–7 mol%) phosphors

Sample	(x, y)	CP (%)	(u', v')	CCT (K)
YPS:1 mol% Er^{3+}	0.3504, 0.4518	83.56	0.1815, 0.5267	5085
YPS:2 mol% Er^{3+}	0.3496, 0.4507	85.04	0.1814, 0.5262	5102
YPS:3 mol% Er^{3+}	0.3505, 0.4500	82.55	0.1821, 0.5261	5081
YPS:4 mol% Er^{3+}	0.3528, 0.4544	87.23	0.1822, 0.5279	5034
YPS:5 mol% Er^{3+}	0.3491, 0.4509	80.19	0.1811, 0.5262	5114
YPS:6 mol% Er^{3+}	0.3472, 0.4476	78.08	0.1809, 0.5248	5156
YPS:7 mol% Er^{3+}	0.3504, 0.4508	79.45	0.1818, 0.5263	5083

$$CCT = -437n^3 + 3601n^2 - 6861n + 5514.31 \quad (19)$$

The formula $n = (x - x_c)/(y - y_c)$ is used, where (x_c, y_c) represents (0.332, 0.186). Calculating the (u', v') coordinates using the given equations is a crucial step, enabling a thorough exploration of the chromaticity characteristics of luminous nanomaterials.[53]

$$u' = \frac{4x}{-2x + 12y + 3} \quad (20)$$

$$v' = \frac{9y}{-2x + 12y + 3} \quad (21)$$

Table 5 lists the CCT values and (u', v') coordinates for the YPS:Er^{3+} (x = 1–7 mol%) phosphors. Each sample demonstrates the correlated color temperature (CCT) values exceeding 5000 K, suggesting their suitability as light sources for producing cool white illumination. This is illustrated in the CCT chart in Fig. S8–S14.†

4 Conclusions

In summary, we utilized a urea-assisted gel-combustion method to produce progressively green glowing $Y_2Si_2O_7$:Er^{3+} phosphors. These phosphors endured comprehensive characterization, including structural, morphological, optical, photoluminescence, temperature-dependent luminescence and colorimetric analyses. The synthesized phosphors exhibited a triclinic phase with space group $P\bar{1}$, and TEM revealed nearly spherical particles ranging from 25–45 nm. EDX spectra confirmed the effective assimilation of Er^{3+} ions into the YPS host matrix. The phosphors displayed a strong emission peak at 548 nm, corresponding to the characteristic $^4S_{3/2} \rightarrow {}^4I_{15/2}$ transition, when excited by a wavelength of 379 nm. This results in a vibrant green luminescence. Notably, the optimal luminescence occurred at 4 mol% Er^{3+} content, with concentration quenching observed beyond this level due to dipole–dipole interactions. Decay lifetimes decreased from 4.3492 to 2.9420 ms with increasing dopant ion concentration. Optical band gap analysis yielded a value of 5.80 eV for the YPS:4 mol% Er^{3+} phosphor, indicating a broad band gap material. Moreover, the phosphors emitted green light with high color purity within the suitable CIE zone. Overall, these phosphors exhibit promising characteristics for applications requiring thermally stable light-emitting diodes.

Data availability

Data will be made available on request.

Author contributions

Pawan Kumar: data curation, writing – original draft, investigation, methodology; Devender Singh: writing – review & editing, resources, supervision; Sitender Singh: validation; Harish Kumar: software; Ramesh Kumar: visualization.

Conflicts of interest

The authors declare that they have no known competing financial interests or personal relationships that could have appeared to influence the work reported in this paper.

Acknowledgements

Pawan Kumar is thankful to UGC-New Delhi for providing SRF [117/(CSIRNETJUNE2019)]. Devender Singh is grateful to MDU, Rohtak, for the Post Seed Grant under the research promotion scheme.

References

1 H. Chander, Development of nanophosphors—A review, *Mater. Sci. Eng., R*, 2005, **49**, 113–155, DOI: 10.1016/j.mser.2005.06.001.
2 I. Gupta, S. Singh, S. Bhagwan and D. Singh, Rare earth (RE) doped phosphors and their emerging applications: A review, *Ceram. Int.*, 2021, **47**, 19282–19303, DOI: 10.1016/j.ceramint.2021.03.308.
3 P. Kumar, S. Singh, I. Gupta, V. Kumar and D. Singh, Structural refinement and optical characteristics of single-phase $Gd_3Al_5O_{12}$:Er^{3+} nanophosphors for luminescent applications, *J. Lumin.*, 2022, **252**, 119338, DOI: 10.1016/j.jlumin.2022.119338.
4 V. V. Shanbhag, S. C. Prashantha, T. S. Shekhar, H. Nagabhushana, R. Naik, K. M. Girish and D. S. Prasanna, Enhanced photoluminescence of SiO_2 coated $CaTiO_3$:Dy^{3+}, Li^+ nanophosphors for white light emitting diodes, *Ceram. Int.*, 2021, **47**, 10346–10354, DOI: 10.1016/j.ceramint.2020.11.077.
5 I. Gupta, D. Singh, S. Singh, P. Kumar, S. Bhagwan and V. Kumar, Structural and luminescent features of warm reddish-orange light-emitting Sm(III) doped $Gd_2Si_2O_7$ nanophosphors for near UV-energized LEDs, *J. Lumin.*, 2023, **263**, 20007, DOI: 10.1016/j.jlumin.2023.120007.
6 W. Li, N. Ma, B. Devakumar and X. Huang, Blue-light-excitable broadband yellow-emitting $CaGd_2HfSc(AlO_4)_3$:Ce^{3+} garnet phosphors for white light-emitting diode devices with improved color rendering index, *Mater. Today Chem.*, 2022, **23**, 100638, DOI: 10.1016/j.mtchem.2021.100638.
7 B. Marí, K. C. Singh, P. Cembrero-Coca, I. Singh, D. Singh and S. Chand, Red emitting $MTiO_3$ (M = Ca or Sr)

phosphors doped with Eu^{3+} or Pr^{3+} with some cations as codopants, *Displays*, 2013, **34**, 346–351, DOI: 10.1016/j.molstruc.2021.131802.

8 P. Kumar, S. Singh, I. Gupta, K. Nehra, V. Kumar and D. Singh, Structural and luminescent behaviour of Dy (III) activated $Gd_3Al_5O_{12}$ nanophosphors for white-LEDs applications, *Mater. Chem. Phys.*, 2023, **295**, 127035, DOI: 10.1016/j.matchemphys.2022.127035.

9 D. Liu, X. Yun, P. Dang, H. Lian, M. Shang, G. Li and J. Lin, Yellow/orange-emitting $ABZn_2Ga_2O_7$: Bi^{3+} (A= Ca, Sr; B= Ba, Sr) phosphors: optical temperature sensing and white light-emitting diode applications, *Chem. Mater.*, 2020, **32**, 3065–3077, DOI: 10.1021/acs.chemmater.0c00054.

10 V. Tanwar, S. Singh, I. Gupta, P. Kumar, H. Kumar, B. Mari and D. Singh, Preparation and luminescence characterization of Eu(III)-activated Forsterite for optoelectronic applications, *J. Mol. Struct.*, 2022, **1250**, 131802, DOI: 10.1016/j.molstruc.2021.131802.

11 P. Kumar, D. Singh, I. Gupta, S. Singh, V. Kumar, H. Kumar and S. K. Chhikara, Perovskite $GdAlO_3$:Dy^{3+} nanophosphors: A gel-combustion synthesis, phase evaluation and down conversion luminescent characteristics for lighting applications, *J. Lumin.*, 2022, **252**, 119409, DOI: 10.1016/j.jlumin.2022.119409.

12 P. Dang, D. Liu, Y. Wei, G. Li, H. Lian, M. Shang and J. Lin, Highly efficient cyan-green emission in self-activated $Rb_3RV_2O_8$ (R= Y, Lu) vanadate phosphors for full-spectrum white light-emitting diodes (LEDs), *Inorg. Chem.*, 2020, **59**, 6026–6038, DOI: 10.1021/acs.inorgchem.0c00015.

13 P. Kumar, D. Singh, I. Gupta, S. Singh, S. Nehra and R. Kumar, Combustion derived single phase $Y_4Al_2O_9$: Tb^{3+} nanophosphor: crystal chemistry and optical analysis for solid state lighting applications, *RSC Adv.*, 2023, **13**, 7752–7765, DOI: 10.1039/D3RA00735A.

14 H. Lin, T. Hu, Q. Huang, Y. Cheng, B. Wang, J. Xu and Y. Wang, Non-rare-earth K_2XF_7: Mn^{4+} (X= Ta, Nb): a highly-efficient narrow-band red phosphor enabling the application in wide-color-gamut LCD, *Laser Photon. Rev.*, 2017, **11**, 1700148, DOI: 10.1002/lpor.201700148.

15 J. E. Murphy, F. Garcia-Santamaria, A. A. Setlur and S. Sista, PFS, K_2SiF_6: Mn^{4+}: the Red-line Emitting LED Phosphor behind GE's TriGain Technology Platform, *Dig. Tech. Pap.*, 2015, **46**, 927–930, DOI: 10.1002/sdtp.10406.

16 E. Song, Y. Zhou, X. B. Yang, Z. Liao, W. Zhao, T. Deng and Q. Zhang, Highly efficient and stable narrow-band red phosphor Cs_2SiF_6:Mn^{4+} for high-power warm white LED applications, *ACS Photonics*, 2017, **4**, 2556–2565, DOI: 10.1021/acsphotonics.7b00852.

17 G. Chen, L. Luo, W. Li, J. S. Yu and P. Du, Designing tunable luminescence in Ce^{3+}/Eu^{2+}-codoped $Ca_8Zn(SiO_4)_4Cl_2$ phosphors for white light-emitting diode and optical anti-counterfeiting applications, *Mater. Today Chem.*, 2022, **26**, 101038, DOI: 10.1016/j.mtchem.2022.101038.

18 P. Kumar, D. Singh and H. Kumar, Gel-combustion synthesis, structural and optoelectronic analyses of Tb^{3+} activated $LaSr_2AlO_5$ nanophosphors: A green emitter for displays, *Mater. Sci. Semicond. Process.*, 2024, **174**, 108162, DOI: 10.1016/j.mssp.2024.108162.

19 J. Du, X. Pan, Z. Liu, Y. Jing, B. Wang, L. Luo and P. Du, Highly efficient Eu3+-activated $Ca_2Gd_8Si_6O_{26}$ red-emitting phosphors: a bifunctional platform towards white light-emitting diode and ratiometric optical thermometer applications, *J. Alloys Compd.*, 2021, **859**, 157843, DOI: 10.1016/j.jallcom.2020.157843.

20 I. Gupta, D. Singh, P. Kumar, S. Singh, S. Bhagwan and V. Kumar, Crystallographic and luminescence studies of $Gd_2Si_2O_7$: Er^{3+} nanomaterials for NUV energized lighting applications, *J. Mol. Struct.*, 2023, **1287**, 135595, DOI: 10.1016/j.molstruc.2023.135595.

21 P. Liu, F. Wang and B. Yang, Upconversion/downconversion luminescence of color-tunable Gd_2O_3: Er^{3+} phosphors under ultraviolet to near-infrared excitation, *Solid State Sci.*, 2020, **102**, 106165, DOI: 10.1016/j.solidstatesciences.2020.106165.

22 P. Kumar, S. Singh, I. Gupta, V. Kumar and D. Singh, Preparation and luminescence behaviour of perovskite $LaAlO_3$: Tb^{3+} nanophosphors for innovative displays, *Optik*, 2022, **267**, 169709, DOI: 10.1016/j.ijleo.2022.169709.

23 Y. Zhang, Z. Liang, W. Wang, Y. Lin, R. Tang, J. Wang and R. Yu, Optical properties of yellow-emitting $Sr_3LaNb_3O_{12}$: Dy^{3+} phosphors with an abnormal thermal quenching for white light-emitting diode applications, *J. Mater. Sci.: Mater. Electron.*, 2022, **33**, 26619–26632, DOI: 10.1007/s10854-022-09374-4.

24 J. Sokolnicki, Rare earths (Ce, Eu,Tb) doped $Y_2Si_2O_7$ phosphors for white LED, *J. Lumin.*, 2013, **134**, 600–606, DOI: 10.1016/j.jlumin.2012.07.023.

25 L. Marciniak, D. Hreniak, W. Strek, F. Piccinelli, A. Speghini, M. Bettinelli and F. Priolo, Spectroscopic and structural properties of polycrystalline $Y_2Si_2O_7$ doped with Er^{3+}, *J. Lumin.*, 2016, **170**, 614–618, DOI: 10.1016/j.jlumin.2015.02.015.

26 D. Singh, V. Tanwar, A. P. Simantilleke, S. Bhagwan, B. Mari, P. S. Kadyan and I. Singh, Synthesis and enhanced luminescent characterization of $SrAl_4O_7$:Eu^{2+}, RE^{3+} (RE = Nd, Dy) nanophosphors for light emitting applications, *J. Mater. Sci.: Mater. Electron.*, 2016, **27**, 5303–5308, DOI: 10.1007/s10854-016-4428-2.

27 C. Y. Yang, S. Som, S. Das and C. H. Lu, Synthesis of $Sr_2Si_5N_8$:Ce^{3+} phosphors for white LEDs via efficient chemical vapor deposition, *Sci. Rep.*, 2017, **7**, 45832, DOI: 10.1038/srep45832.

28 J. Miranda de Carvalho, C. C. S. Pedroso, M. S. D. N. Saula, M. C. F. C. Felinto and H. F. D. Brito, Microwave-assisted preparation of luminescent inorganic materials: A fast route to light conversion and storage phosphors, *Molecules*, 2021, **26**, 2882, DOI: 10.3390/molecules26102882.

29 P. Kumar, S. Singh, I. Gupta, V. Kumar and D. Singh, Structural and optical characterization of trivalent samarium-activated $LaAlO_3$ nanocrystalline materials for solid-state lighting, *J. Mol. Struct.*, 2022, **1265**, 133362.

30 R. H. Krishna, B. M. Nagabhushana, B. N. Sherikar, N. S. Murthy, C. Shivakumara and T. Thomas, Luminescence enhancement in monoclinic $CaAl_2O_4$: Eu^{2+},

Cr^{3+} nanophosphor by fuel-blend combustion synthesis, *Chem. Eng.*, 2015, **267**, 317–323, DOI: 10.1016/j.cej.2014.12.102.

31 P. Kumar, D. Singh, I. Gupta, S. Singh, S. Nehra and R. Kumar, A study of phase evolution, crystallographic and down-conversion luminescent behaviour of monoclinic $Y_4Al_2O_9$:Dy^{3+} nanophosphors for white light applications, *Opt. Mater.*, 2023, **138**, 113677, DOI: 10.1016/j.optmat.2023.113677.

32 V. Kahlenberg, W. Wertl, D. M. Többens, R. Kaindl, P. Schuster and H. Schottenberger, Rietveld analysis and raman spectroscopic investigations on α-$Y_2Si_2O_7$, *Z. Anorg. Allg. Chem.*, 2008, **634**, 1166–1172, DOI: 10.1002/zaac.200700548.

33 S. K. Sharma, S. Som, R. Jain and A. K. Kunti, Spectral and CIE parameters of red emitting $Gd_3Ga_5O_{12}$: Eu^{3+} phosphor, *J. Lumin.*, 2015, **159**, 317–324, DOI: 10.1016/j.jlumin.2014.11.010.

34 P. Kumar, D. Singh, I. Gupta and H. Kumar, Influence of Dy^{3+} ion concentration on structural, photoluminescence and energy transfer mechanism of promising $GdSr_2AlO_5$ nanophosphors for white light applications, *Ceram. Int.*, 2023, **49**, 29010–29024, DOI: 10.1016/j.ceramint.2023.06.173.

35 S. K. Pathak, A. Verma and A. Verma, Structural and photoluminescence properties of Eu^{3+} activated $ZnAl_2O_4$ orange-red phosphor, *J. Mater. Sci.: Mater. Electron.*, 2020, **31**, 16137–16149, DOI: 10.1007/s10854-020-03715-x.

36 A. Mondal and J. Manam, Structural, optical and temperature dependent photoluminescence properties of Cr^{3+}-activated $LaGaO_3$ persistent phosphor for optical thermometry, *Ceram. Int.*, 2020, **46**, 23972–23984, DOI: 10.1016/j.ceramint.2020.06.174.

37 P. Kumar, D. Singh and I. Gupta, UV excitable $GdSr_2AlO_5$:Eu^{3+} red emitting nanophosphors: Structure refinement, photoluminescence, Judd-Ofelt analysis and thermal stability for w-LEDs, *J. Alloys Compd.*, 2023, **966**, 171410, DOI: 10.1016/j.jallcom.2023.171410.

38 I. Gupta, D. Singh, S. Singh, P. Kumar, S. Bhagwan and V. Kumar, Structural and photophysical measurements of Er^{3+} doped $Gd_4Al_2O_9$ nanophosphors for NUV excitable solid-state lighting applications, *Chem. Phys. Lett.*, 2023, **814**, 140350, DOI: 10.1016/j.cplett.2023.140350.

39 I. Gupta, P. Kumar, S. Singh, S. Bhagwan, S. K. Chhikara and D. Singh, Crystal configuration, spectroscopic and optical characteristics of Er^{3+} doped $YAlO_3$ perovskites for advanced photonic appliances, *Inorg. Chim. Acta*, 2022, **543**, 121183, DOI: 10.1016/j.ica.2022.121183.

40 R. Reddappa, L. L. Devi, P. Babu, I. R. Martín, V. Lavín, V. Venkatramu and C. K. Jayasankar, Structural, morphological and photoluminescence properties of Ca_2SiO_4: Er^{3+} phosphors synthesized from agro-food waste materials, *Ceram. Int.*, 2022, **48**, 37013–37019, DOI: 10.1016/j.ceramint.2022.08.271.

41 Y. Liu, Y. Liu, G. Liu, X. Dong and J. Wang, Up/down conversion, tunable photoluminescence and energy transfer properties of $NaLa(WO_4)_2$: Er^{3+}, Eu^{3+} phosphors, *RSC Adv.*, 2015, **5**, 97995–98003, DOI: 10.1039/C5RA17370A.

42 R. A. Talewar, S. K. Mahamuda, A. S. Rao and S. V Moharil, Intense infrared emission of Er^{3+} in ZnB_2O_4 phosphors from energy transfer of Bi^{3+} by broadband UV excitation, *J. Lumin.*, 2022, **244**, 118706, DOI: 10.1016/j.jlumin.2021.118706.

43 I. Gupta, P. Kumar, S. Singh, S. Bhagwan, V. Kumar and D. Singh, Phase recognition, structural measurements and photoluminescence studies of reddish-orange-emissive $YAlO_3$: Sm^{3+} perovskite nanophosphors for NUV energized WLEDs, *J. Mol. Struct.*, 2022, **1267**, 133567, DOI: 10.1016/j.molstruc.2022.133567.

44 P. Kumar, D. Singh and I. Gupta, Physical insights into crystal structure and optical response of green light emitting Tb^{3+} activated $GdSr_2AlO_5$ nanophosphors for optical displays, *Mater. Res. Bull.*, 2023, **167**, 112413, DOI: 10.1016/j.materresbull.2023.112413.

45 P. Kumar, D. Singh, I. Gupta, S. Singh, S. Nehra and R. Kumar, Realization of warm reddish-orange light emitter single phase $Y_4Al_2O_9$:Sm^{3+} nanophosphors for indoor lighting applications, *J. Lumin.*, 2023, **257**, 119703, DOI: 10.1016/j.jlumin.2023.119703.

46 K. Nehra, A. Dalal, A. Hooda, K. Jakhar, D. Singh and S. Kumar, Preparation, optoelectronic and spectroscopic analysis of fluorinated heteroleptic samarium complexes for display applications, *Inorganica Chim. Acta*, 2022, **537**, 120958, DOI: 10.1016/j.ica.2022.120958.

47 D. Gao, Y. Li, L. Cheng, S. Liu, S. Xu, X. Li and B. Chen, Concentration effects of fluorescence quenching and optical transition properties of Dy^{3+} doped $NaYF_4$ phosphor, *J. Alloys Compd.*, 2022, **895**, 162616, DOI: 10.1016/j.jallcom.2021.162616.

48 S. P. Ghorpade, R. H. Krishna, R. M. Melavanki, V. Dubey and N. R. Patil, Effect of Eu^{3+} on optical and energy bandgap of SrY_2O_4 nanophosphors for FED applications, *Optik*, 2020, **208**, 164533, DOI: 10.1016/j.ijleo.2020.164533.

49 N. M Bhiri, M. Dammak, M. Aguilo, F. Diaz, J. J. Carvajal and M. C. Pujol, Stokes and anti-Stokes operating conditions dependent luminescence thermometric performance of Er^{3+}-doped and Er^{3+}, Yb^{3+} co-doped $GdVO_4$ microparticles in the non-saturation regime, *J. Alloys Compd.*, 2020, **814**, 152197, DOI: 10.1016/j.jallcom.2019.152197.

50 P. Kumar, D. Singh, I. Gupta and H. Kumar, Synthesis, crystallographic structure, down shifting luminescence of Er(III) activated $GdSr_2AlO_5$ nanophosphors: An efficient green emitter for solid state lighting, *Mater. Sci. Semicond. Process.*, 2023, **167**, 107765, DOI: 10.1016/j.mssp.2023.107765.

51 P. Kumar, S. Singh, I. Gupta, A. Hooda, V. Kumar and D. Singh, Reddish-orange color tunable Sm^{3+} activated $Gd_3Al_5O_{12}$ phosphors: crystallographic and photophysical investigation for lighting applications, *J. Mol. Struct.*, 2023, **1271**, 134074, DOI: 10.1016/j.molstruc.2022.134074.

52 P. Kumar, S. Singh, I. Gupta, A. Dalal, V. Kumar and D. Singh, Preparation, structural and photometric properties of single-phased $Gd_3Al_5O_{12}$:Tb^{3+} green-emitting

phosphors for solid state lighting purpose, *Mater. Sci. Eng., B*, 2023, **288**, 166189, DOI: **10.1016/j.mseb.2022.116189**.

53 P. Kumar, D. Singh and H. Kumar, Red-emitting Eu^{3+} activated $LaSr_2AlO_5$ phosphor for wLEDs: Crystal structure, photoluminescence, thermal stability, Judd-Ofelt calculation and band-gap analyses, *Mater. Res. Bull.*, 2024, **173**, 112683, DOI: **10.1016/j.materresbull.2024.112683**.